



# High-quality and large-area echelle grating ruled on 500-mm ruling engine for the fiber array solar optical telescope (FASOT)

XIAOTAO MI,\*  XIANGDONG QI, SHANWEN ZHANG, HONGZHU YU, SIBO JIANG, AND JINGXUAN ZHOU

*Changchun Institute of Optics, Fine Mechanics and Physics, Chinese Academy of Sciences, Changchun, Jilin 130033, China*

\*[mixiaotao@ciomp.ac.cn](mailto:mixiaotao@ciomp.ac.cn)

**Abstract:** A 300 mm×500 mm large-area echelle grating with groove density of 79 grooves/mm is fabricated for the spectrometer of the fiber array solar optical telescope (FASOT). This paper focusses on measurement methods of the grating performance. We present a method to evaluate the grating's stray light intensity, which is measured to a level of  $10^{-4}$ . The directly measured grating efficiency is approximately 90% of the designed value, and an indirect measurement method based on the grating groove profile is proposed. Based on the Rayleigh criterion and the grating diffraction wavefront, a physical optics method and a geometric grating method are proposed and are used to calculate the actual grating resolving power; the calculated results exceed 95% of the grating's theoretical resolving power. These results show that the CIOMP-6 ruling engine has sufficient precision to fabricate high-quality, large-area echelle gratings.

© 2021 Optical Society of America under the terms of the [OSA Open Access Publishing Agreement](#)

## 1. Introduction

The excellent functionality of large-area gratings, which includes their high resolving power and light collection capabilities, has led to strong demand for these elements for use in applications ranging from large-scale optical telescopes [1–3] to inertial confinement fusion (ICF) systems [4–6] and deep ultraviolet light sources for mask aligners [7]. The mechanical ruling method, which is one of the most important ways to produce gratings, is mainly used to fabricate large-area echelle gratings and infrared gratings with deep grooves and high-quality shapes [8–10]. Development of both ruling engines and ruled gratings has been in progress for more than a century, but the pursuit of larger scales and higher precision in both the ruling engines and the ruled gratings to meet their application requirements continues [11–14].

The development of interferometry techniques and closed-loop control technology and their application to ruling engines have made it possible to develop high-quality and large-sized ruling engines and ruled gratings [15,16]. The internationally known large grating ruling engines that have been reported in the literature to date include the MIT-C engine from the United States, the Hitachi-4 engine from Japan, and the CIOMP-6 engine from China. The MIT-C engine uses a continuous-motion system with closed-loop interference control, can rule blanks with dimensions ranging up to 450 mm×650 mm, and has ruled a wide variety of high-precision gratings with dimensions of up to 350 mm×450 mm [17,18]. The Hitachi-4 engine uses a new type of stop-and-go operation, allowing it to fabricate ruled gratings with maximum dimensions of 300 mm×200 mm, and this engine has demonstrated a highest groove density of 10,000 grooves/mm [19].

The CIOMP-6 ruling engine is based on a new concept involving the inclusion of a new diamond carriage system that uses a flexible wire rope to drive the aerostatic guideways, a new groove positioning method based on adjustment of the position of the diamond, a new groove error measurement method, and high-precision control concepts and strategies. The engine has

demonstrated its ability to rule high-density gratings with the highest groove density ranging up to 8000 grooves/mm and large-area gratings with a maximum ruled area of 400 mm×500 mm on the blank [20,21].

Since completion of the development of CIOMP-6, numerous high-quality gratings have been fabricated, including high-efficiency gratings with 500, 768 and 1520 grooves/mm, a 64.285 grooves/mm echelle grating with a high-precision shape, 11.904 and 12.820 grooves/mm infrared gratings, and a 300 mm×500 mm large-area echelle grating with a groove density of 79 grooves/mm [21]. The most difficult grating to fabricate to date is the 300 mm×500 mm large-area echelle grating for the spectrometer mounted on the Fiber Arrayed Solar Optical Telescope (FASOT), which was designed by the Yunnan Observatory of the Chinese Academy of Sciences.

In this work, we briefly introduce the requirements for and the fabrication processes of these gratings and focus on measurement methods of the grating performance. Based on the distribution of the stray light from the grating, we propose a method to evaluate and measure this stray light. Two methods are used to evaluate the grating diffraction efficiency. The first is a direct measurement approach, and in the second, the grating efficiency is calculated from the grating groove profile. The indirect measurement method to obtain the grating efficiency based on the grating groove profile is proposed that provides a new concept and method for acquisition of the diffraction efficiency of a grating when the grating efficiency cannot be measured directly. Finally, based on the grating's diffraction wavefront, we propose a physical optical method and a geometric grating method to calculate the actual grating resolving power.

## **2. Brief introduction of grating requirements and the grating fabrication process**

The Fiber Array Solar Optical Telescope (FASOT) is a new solar telescope designed by Zhongquan Qu's team at the Yunnan Observatory of the Chinese Academy of Sciences. One unique feature of the FASOT is that it will be capable of performing real-time, high-efficiency, and high-precision spectral imaging polarimetry of multiple magneto-sensitive lines over a two-dimensional field of view, i.e., performing real-time 3D Stokes measurements of multiple lines. Therefore, because it acts as a highly efficient 3D spectropolarimeter, the FASOT will be capable of realizing very high temporal resolution, which will permit accurate mapping of the magnetic field, the line-of-sight velocity, and the thermodynamic parameters at multiple scale heights in the solar atmosphere. Simultaneously, space weather monitoring, catastrophic space weather forecasting, and early warnings can be provided by combining the FASOT with large-field observation instruments [22–24].

To allow the FASOT to perform its expected functions, the FASOT development team has undertaken a great deal of innovative work. The optical path of the FASOT differs from the typical paths used in telescopes; see [24] for further information. The solar light is collected via the guiding optics of the main telescope and then inputted to a field stop located at the Cassegrain focus plane of the main telescope that splits the field of view (FOV) into two parts. The smaller part (0.5'×0.5') passes the light directly into the polarimetric system to perform the polarimetric measurements, and the remaining part of the FOV is reflected vertically and used in the monitoring system. Subsequently, the light that is modulated by the polarimeter is split into two beams with opposite polarization states and these beams are then transmitted into integral field spectrometers and their detectors using an integral field unit (IFU) with optical fibers to conduct two-beam spectro-imaging polarimetry. Considering that the optical fiber used is not a polarization maintaining optical fiber, the light incident into the spectrometers is treated as non-polarized light. To achieve the large FOV required, the FASOT system uses six integral field spectrometers, which in turn will require six high-quality and large-area echelle gratings. Table 1 summarizes the specifications for these FASOT echelle gratings.

**Table 1. FASOT Echelle Grating Specifications**

Item	Detail
Groove density	79groove/mm
Wavelengths of interest	516~525nm
Ruling area	300mm×500mm
Blaze order	-43
Efficiency	About 90% of the theoretical value
The intensity of stray light	$10^{-4}$ level of incident light
Resolving power of grating	550000@520nm

The main factors that affect the grating quality include the operating accuracy of the grating ruling engine and the grating ruling technology used. The operating accuracy of the ruling machine has a comprehensive impact on the ruling grating. Specifically, the groove position error will affect the grating groove density; the random error components at medium and high frequencies in the groove position error will generate stray light and affect the grating groove shape precision; the periodic groove position errors will generate ghosts; and the low frequency components of the groove position error affect the grating diffraction wavefront, which then affects the resolving power of the grating. The ruling technology mainly affects the grating groove shape, which then affects the diffraction efficiency of the grating.

The CIOMP-6 ruling engine uses interferometric measurement technology and piezoelectric ceramics for nanoscale positioning to realize the root-mean-square (RMS) value of groove position errors less than 3 nm. In addition, drawing on more than 60 years of ruling technology experience, the basic conditions for grating development have been obtained. Even under the mature conditions described above, we still required an entire year to explore the fabrication process for these large gratings, and we then fabricated large gratings that met the requirements described above for the first time. A photograph of the gratings is shown in Fig. 1.

**Fig. 1.** Photograph of the gratings.

### 3. Measurement of grating performance

Among the grating specifications given in Table 1, the ruling area is mainly determined by the engine's operating range and can be measured using a vernier caliper, which will not be described here. With regard to the stray light intensity, we will first define this intensity and then measure the stray light intensity of the grating. The grating groove density, the wavelength of interest, and the diffraction order are no longer described separately and will be mentioned in the discussion of the grating diffraction efficiency. At present, we do not have an instrument available to measure the resolving power of the grating. We will thus calculate the actual grating resolving power indirectly from the results of measurement of the grating diffraction wavefront.

#### 3.1. Intensity of the stray light

The development of interferometry methods, closed-loop control technologies, and macro-micro positioning systems and the application of these technologies to ruling engines allowed the grating groove positions to be determined based on the wavelength of the light. The various ghosts caused by the periodic error components in the groove position error are not obvious, and the emission of stray light caused by the random error components of the groove error has been improved greatly.

The stray light extends more or less continuously from one diffracted order to the next, and is mainly concentrated within the vicinity of the blazed order (i.e., the order in which the grating is used) of the grating. Measurements of the stray light can, in principle, be performed using any form of spectrometer; the simplest method is to measure it in an instrument using the grating to be measured. However, if the performance of the grating itself is to be measured, rather than that of the instrument as a whole, it will be necessary to take particular care to ensure that the stray light that is detected originates solely from the grating and not from any other parts of the instrument. The measurement results for the stray light vary with use of different instruments and different grating types. It is thus evident that it is very difficult to provide a quantitative specification for the stray light in a manner that would enable the performance of a grating in one instrument to be predicted using measurements acquired using a single instrument. Therefore, there is no generally accepted convention by which different manufacturers can measure and specify the stray light performances of their gratings.

The echelle grating has a wide-band range, and the stray light at other wavelengths can be deduced theoretically by evaluating the stray light level of the grating at a single wavelength. Therefore, it is not necessary to evaluate the stray light at each wavelength, and the red light at 632.8 nm is generally selected as the wavelength for the stray light measurements. In addition, there are many echelle grating diffraction orders, which means that it is not advisable to measure all the stray light between each of the pairs of orders. Because the stray light is mainly distributed near the grating diffraction order, the grating stray light measurement scheme is as shown in Fig. 2. The laser is reflected from a point near the top edge of a mirror onto the grating, and the grating is then aligned to put the blazed order into the Littrow condition, where the incidence angle and diffraction angle are the same. The grating is also tilted out of plane by 0.4°, thus allowing diffracted rays and stray light to pass above the top edge of the mirror and then be measured using a power meter. The power meter was used to measure the intensity  $I_1$  of the incident laser beam at position 1, along with the intensities  $I_2$  and  $I_3$  of the stray light at positions 2 and 3, respectively, near the blazed order, which allows the grating intensity of the stray light to be defined as:

$$I_{st} = \frac{I_2 + I_3}{I_1}. \quad (1)$$

To reflect the overall grating performance comprehensively, we measured multiple points at different positions. The measured results obtained show that the stray light intensity of the grating differs slightly at the different positions on the surface, although all values are at a level of  $10^{-4}$ .

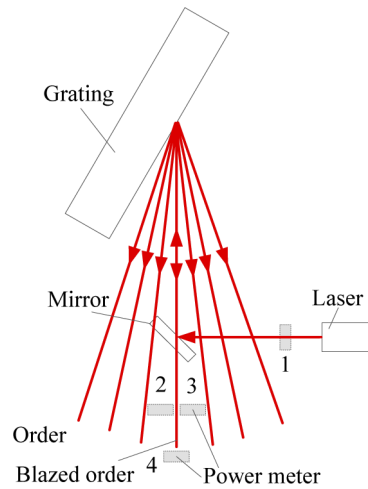


**Fig. 2.** Schematic of process for grating stray light and efficiency measurements.

### 3.2. Grating efficiency

The grating diffraction efficiency is determined by the grating groove shape; the groove shape of the blazed grating is triangular, and the main factors that affect the efficiency of this grating are the blaze angle (i.e., the angle between the working facet in the triangular groove shape and the grating surface) and the grating groove depth.

The methods that can be used to obtain the grating diffraction efficiency can be divided into a direct method and an indirect method. The direct method involves measuring the grating diffraction efficiency according to the design requirements, while the indirect method involves calculating the grating diffraction efficiency by obtaining the grating groove profile. For the indirect measurement method, the grating groove profile can be measured using an atomic force microscope (AFM) or a scanning electron microscope (SEM).

#### 3.2.1. Direct method

As shown in Fig. 2, the schematic of the grating efficiency measurement setup is basically the same as the schematic of the grating stray light measurement setup, except that the laser selected is a tunable laser. The grating diffraction order can be counted, and the wavelength of interest is the band in which efficiency needs to be measured. The power meter was used to measure the incident laser intensity  $I_1$  at position 1, along with the intensity  $I_4$  of the blazed order ( $-43rd$ ) of the grating at position 4, which means that the grating intensity of the stray light can be defined as:

$$I_e = \frac{I_4}{I_1}. \quad (2)$$

As with the stray light measurement procedure, we also measured several points at different locations on the grating and found no significant differences in efficiency between the front and rear ends of the grating. The measured grating diffraction efficiency results are shown in Fig. 4, and measurement point in the figure is the average of measurements in different locations.

#### 3.2.2. Indirect method

The grating efficiency is generally expected to be obtained via direct measurements, but it may be difficult to do so in certain cases, particularly in the ultraviolet and infrared bands. The groove shape was measured using an AFM, with results as shown in Fig. 3. For comparison purposes,

we have listed the measured and theoretical values of the grating shape parameters as shown in Table 2.

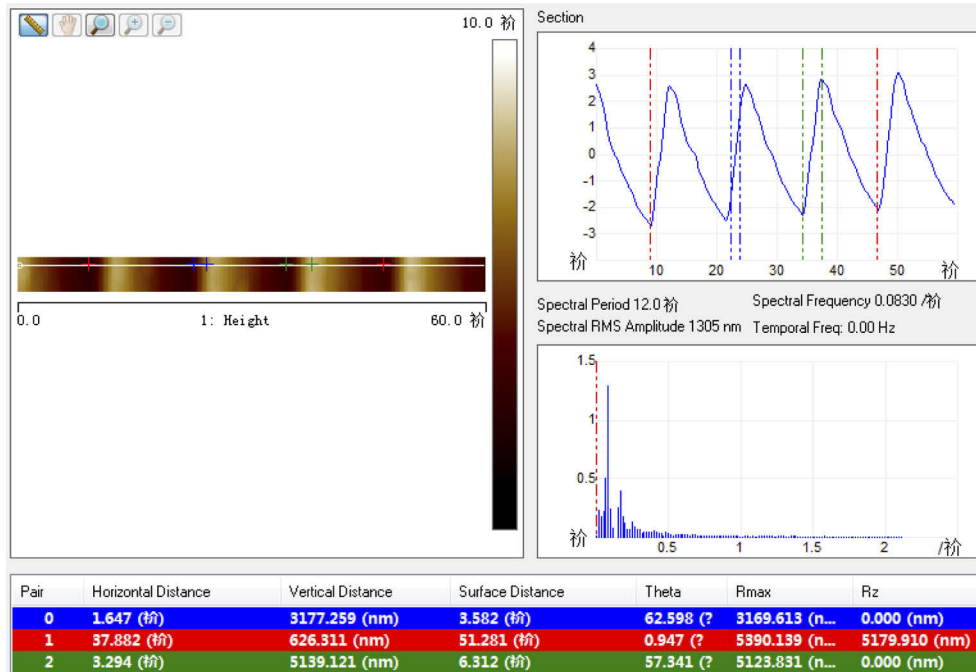


**Fig. 3.** Atomic force microscope test results of grating.

**Table 2. Designed and measured values of the 64.285 grooves/mm grating.**

Parameter	Design Value	Measured Value
Grating period (the reciprocal of the grating groove density)	12658.2nm	12627.3nm
Groove depth	5165.4nm	5139.121nm
Blaze angle	62.65°	62.598°

According to the results in Fig. 3 and the specifications in Table 1, the following conclusions can be drawn: the difference between the measured and theoretical grating periods (i.e., the reciprocal of the grating groove density) is mainly caused by the image pixel size (i.e., the number of pixels at the same measurement distance determines the resolution of measurement), and the actual grating period is closer to the theoretical value; the blazed angle obtained from the grating measurement points is 62.598°, but the blazed angles at different measurement points within the same groove differ slightly; the blazed surface of the grating is relatively flat and the nonblazed surface is irregular, but this has little effect on the grating diffraction efficiency [9]. We entered the measured grating groove parameters into grating calculation software, and the grating diffraction efficiency was then calculated with results as shown in Fig. 4.

As shown in Fig. 4, the measured efficiency of the grating is approximately 90% of the designed efficiency. The grating efficiency curve calculated based on the grating groove profile can basically reflect the actual grating diffraction efficiency, but its value is lower than that of the measured efficiency, mainly because a single grating profile cannot reflect the actual grating efficiency accurately. As shown in Fig. 3, no two grooves are the same. We believe that if enough

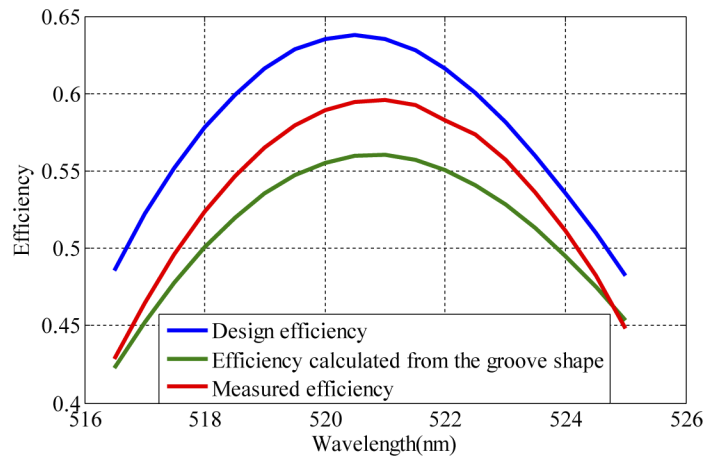


**Fig. 4.** Grating efficiencies obtained by different methods.

grating groove data are collected, the calculated grating efficiency from the groove shape will be very close to the measured grating efficiency, which of course requires considerable work.

### 3.3. Grating resolving power

The large area of the grating is mainly used to obtain higher resolving powers and a stronger ability to collect light. The resolving power of the spectral instrument is required to be 110,000, and the resolving power of the grating is required to be 550,000. Using the Rayleigh criterion, the theoretical resolving power is found to be equal to the total number of wavelengths contained within the optical path difference between the diffracted light components from the two grating edges and is calculated to be 1,698,500.

It is actually quite difficult to measure the resolving powers of gratings. The most important thing is to test the grating using an instrument that does not introduce any significant aberrations. Otherwise, the instrument itself will distort the spectral image, thus meaning that the results will be reliable only for this instrument, and these results will be irrelevant if the same grating is used on a different instrument. At present, we do not have an instrument to measure the general resolving power of gratings, and thus we can only evaluate the grating resolving power via indirect measurements.

The grating resolving power corresponds to the quality of the diffraction wavefront from that grating. The grating diffraction wavefront can be measured using the Zygo interferometer. Therefore, the grating's resolving power will be estimated using the diffraction wavefront of the grating. Specifically, there are two possible methods, which are described as follows: the first is the physical optics method, i.e., the complex amplitude distribution of the grating diffraction spectrum can be obtained based on the grating diffraction wavefront, and the resolving power of the grating can then be estimated; the second method is the geometric optics method, which uses the ray tracing method to obtain the spot diagram of the light that passes through the grating to estimate the resolving power of the grating.

The Zygo interferometer measurement results for the grating at 632.8 nm, with a blazed order of  $-35$ , are shown in Fig. 5. Figure 5(a) shows that the peak-to-valley (PV) values and root-mean-square (RMS) values for the entire grating are  $0.294\lambda$  and  $0.037\lambda$ , respectively; Fig. 5(b) shows the PV and RMS values of one of the cross-sectional profiles along the grating dispersion direction, which are  $0.135\lambda$  and  $0.031\lambda$ , respectively. As shown in Fig. 5(c), the point spread function (PSF) indicates that the diffracted energy is concentrated at the central spot, and

the Strehl ratio is 0.943. Figure 5(d) shows the fringes when they are oriented parallel to the grooves, and Fig. 5(e) shows the corresponding fringes when they are oriented perpendicular to the grooves.

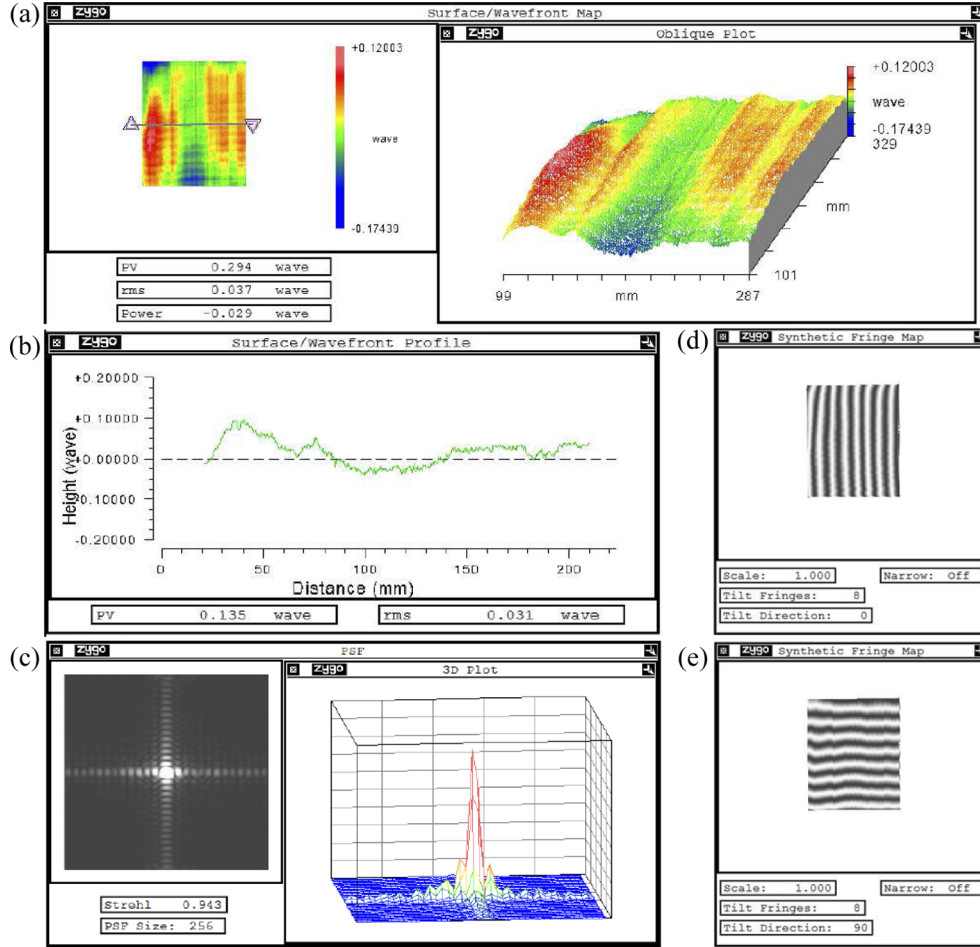


**Fig. 5.** Wavefront quality of the grating. (a) Peak-to-valley (PV) and root-mean-square (RMS) values of the entire grating wavefront obtained from 2D and 3D wavefront maps ; (b) PV and RMS values for one of the cross-sectional profiles along the dispersion direction of the grating; (c) point spread function (PSF) of the grating; (d) fringes oriented parallel to the grooves; and (e) fringes oriented perpendicular to the grooves.

### 3.3.1. Physical optics method

We assume here that each point in the diffraction wavefront has the same complex amplitude value. The normalized coordinates of the diffraction wavefront are  $\eta$  ( $|\eta| \leq 1$ ) and  $\xi$  ( $|\xi| \leq 1$ ). The angular coordinates of the grating's diffraction spectrum are  $u$  and  $v$ . The wavelength dispersion of the grating occurs along the directions of  $\eta$  and  $\xi$ . The complex amplitude of the grating's diffraction spectrum can then be expressed as

$$E(u, v) = C \int_{-1}^1 \int_{-1}^1 e^{ik\Delta(\eta, \xi)} e^{i(u\eta + v\xi)} d\eta d\xi \quad (3)$$

where  $C$  is a constant, and  $\Delta(\eta, \xi)$  is the grating diffraction wavefront.

The normalized complex amplitude of the grating diffraction spectrum can then be expressed as:

$$A(u, v) = \frac{1}{4} \int_{-1}^1 \int_{-1}^1 e^{ik\Delta(\eta, \xi)} e^{i(u\eta + v\xi)} d\eta d\xi. \quad (4)$$

According to Eq. (4), the normalized diffraction intensity of the grating's diffraction spectrum  $I$  can be given by:

$$I = A(u, v)A^*(u, v). \quad (5)$$

Using Eq. (5), we can then obtain the first minimum half-angle width  $u_{min}$  of the diffraction spectrum distribution. According to the Rayleigh criterion, the ratio  $R_1$  of the real resolution power to the ideal resolving power of the grating can be expressed as:

$$R_1 = \frac{\pi}{u_{min}}. \quad (6)$$

By substituting the wavefront data from Fig. 5 into Eqs. (3)–(5), the intensity distribution of the diffraction spectrum of the actual grating can be obtained as shown in Fig. 6, where  $u$  and  $v$  are the angular coordinates of the grating diffraction spectrum, and  $u$  is the wavelength dispersion direction of the grating. Figure 7 shows the intensity distribution for the diffraction spectrum when  $v=0$ . From Fig. 6 and Fig. 7, we can determine that the grating has very high resolving power and a resolving power ratio  $R_1$  that exceeds 99%.

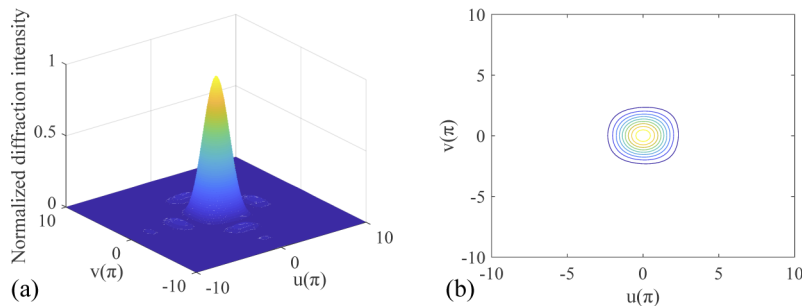


**Fig. 6.** Intensity distributions of the grating diffraction spectrum. (a) Three-dimensional distribution; and (b) contour distribution.

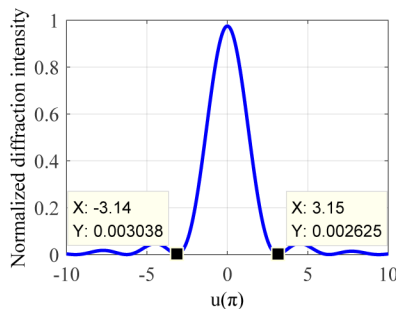


**Fig. 7.** Intensity distribution of the grating diffraction spectrum (when  $v=0$ ).

### 3.3.2. Geometrical optics method

The schematic diagram of the optical path used to calculate the resolving power of the grating using the geometric optics method is shown in Fig. 8. We assume that the grating is used in the

Littrow condition, the focal length of the focusing lens is  $f$ , and the ray tracing method is used to determine the spot diagram of the ray after it passes through the grating; the RMS width  $r_u$  in the direction of dispersion of the tracing points in the diagram can then be obtained.

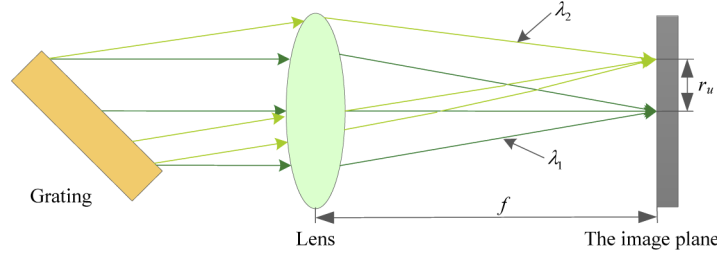


**Fig. 8.** Schematic diagram of the optical path used to calculate the grating resolving power.

The grating diffraction equation is given as follows:

$$d \times (\sin \theta_i + \sin \theta_d) = m\lambda \tag{7}$$

where  $d$  is the grating constant,  $m$  is the grating diffraction order,  $\theta_i$  is the angle of incidence,  $\theta_d$  is the diffraction angle, and  $\lambda$  is the working wavelength.

The grating resolving power is expressed as:

$$Rp = \frac{\lambda}{\Delta\lambda}. \tag{8}$$

According to the Rayleigh criterion, by combining Eqs. (7) and (8), the grating resolution in the case shown in Fig. 6 can be given as:

$$Rp = \frac{m\lambda}{d \left\{ \frac{m\lambda}{2d} + \sin \left[ \arctan\left(\frac{r_u}{f}\right) + \arcsin\left(\frac{m\lambda}{2d}\right) \right] \right\} - m\lambda}. \tag{9}$$

As shown in Fig. 8, the lens focal length is set at 1000 mm without consideration of the aberration caused by the lens, and a rectangular beam that can cover the entire grating area is

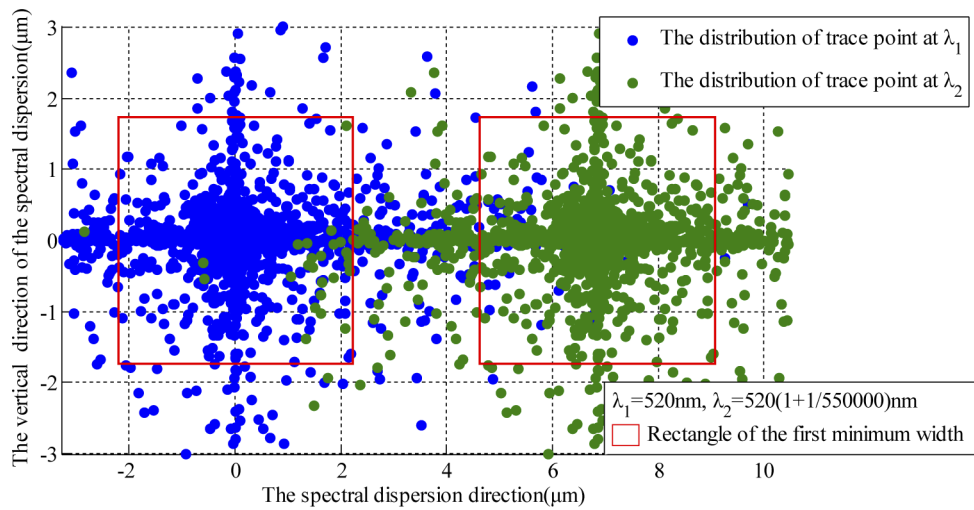


**Fig. 9.** Spot diagrams for  $\lambda_1$  (520 nm) and  $\lambda_2$  (520 + 520/550000 nm).

used. The spot diagrams obtained at  $\lambda_1$  (520 nm) and  $\lambda_2$  (520 + 520/550000 nm) are shown in Fig. 9.

As shown in Fig. 9, the degree of dispersion of the ray tracing points in the spectral dispersion direction is more serious than that in the direction vertical to the spectral dispersion direction, and the ray tracing points are mainly distributed within the rectangle of the first minimum width.

The RMS width  $r_u$  in the dispersion direction is determined to be 2.2827  $\mu\text{m}$ , which is slightly larger than the theoretical value of 2.2177  $\mu\text{m}$ ; substitution of the data into Eq. (9) allows the value of the real resolving power of 1,633,800 to be determined, which meets the requirements given in Table 1.

#### 4. Conclusions

The requirements for and fabrication of a 300 mm $\times$ 500 mm large-area echelle grating with a groove density of 79 grooves/mm are briefly introduced, and the grating performance measurement method is studied in depth. Based on the actual distribution characteristics of the stray light from the grating, we propose an evaluation method for the stray light from the grating, and measured the stray light intensity over the entire grating to be at a level of  $10^{-4}$ . Two methods were used to evaluate the grating diffraction efficiency. The first was a direct measurement approach, and in the second, the grating efficiency was calculated from the grating groove profile. The directly measured grating efficiency was approximately 90% of the theoretical value, which was slightly higher than the efficiency calculated using the second method. According to the Rayleigh criterion and using the grating diffraction wavefront, we propose a physical optics method and a geometric grating method to calculate the actual grating resolution. The calculated results show that the actual grating resolving power is more than 95% of the theoretical value.

In conclusion, the fabricated grating can meet its application requirements, and the CIOMP-6 grating ruling engine has demonstrated its capability for development of high-quality and large-area echelle gratings.

**Funding.** Ministry of Science and Technology of the People's Republic of China (2016YFF0102006); National Natural Science Foundation of China (62005273).

**Acknowledgments.** The authors would like to thank Prof. Zhongquan Qu for placing their trust in us and for selecting us to fabricate the gratings that they required. We thank David MacDonald, MSc, from Liwen Bianji (Edanz) (<https://www.liwenbianji.cn/>) for editing the English text of a draft of this manuscript.

**Disclosures.** The authors declare no conflicts of interest.

**Data availability.** Data underlying the results presented in this paper are not publicly available at this time but may be obtained from the authors upon reasonable request.

#### References

1. S. Mahadevan, L. Ramsey, J. Wright, M. Endl, S. Redman, C. Bender, A. Roy, S. Zonak, N. Troupe, L. Engel, S. Sigurdsson, A. Wolszczan, and B. Zhao, "The habitable zone planet finder: a proposed high-resolution NIR spectrograph for the Hobby Eberly Telescope to discover low-mass," *Proc. SPIE* **7735**, 77356X (2010).
2. G. De Marchi, M. B. J. te Plate, S. M. Birkmann, T. Böker, P. Ferruit, G. Giardino, P. Jakobsen, M. Sirianni, J.-C. Savignol, X. Gnata, R. Barho, M. Kosse, P. Mosner, B. Dörner, G. Cresci, F. Rosales-Ortega, M. Tuhlinger, T. Gross, and T. Leikert, "Calibrating the position of images and spectra in the NIRSpec instrument for the James Webb Space Telescope," *Proc. SPIE* **8150**, 81500C (2011).
3. T. Sakanoi, Y. Kasaba, M. Kagitani, H. Nakagawa, J. Kuhn, and S. Okana, "Development of infrared Echelle spectrograph and mid-infrared heterodyne spectrometer on a small telescope at Haleakala, Hawaii for planetary observation," *Proc. SPIE* **9147**, 91478D (2014).
4. J. Qiao, A. Kalb, T. Nguyen, J. Bunkenburg, D. Canning, and J. H. Kelly, "Demonstration of large-aperture tiled-grating compressors for high-energy, petawatt-class, chirped-pulse amplification systems," *Opt. Lett.* **33**(15), 1684–1686 (2008).
5. A. Cotel, C. Crotti, P. Audebert, C. Le Bris, and C. Le Blanc, "Tiled-grating compression of multiterawatt laser pulses," *Opt. Lett.* **32**(12), 1749–1751 (2007).
6. Y. Ezaki, M. Tabata, M. Kihara, Y. Horiuchi, M. Endo, and T. Jitsuno, "Development of a segmented grating mount system for FIREX-1," *Proceedings of the fifth International Conference on Inertial Fusion Sciences and Applications*, J. Phys. Conf. Ser. 112(3), 032027 (2008).

7. H. Endert, R. Patzel, U. Rebhan, M. Powell, and D. Basting, "New KrF and ArF Excimer Lasers for Advanced Deep Ultraviolet Optical Lithography," *Jpn. J. Appl. Phys.* **34**(Part 1, No. 8A), 4050–4054 (1995).
8. X. Mi, S. Zhang, X. Qi, H. Yu, J. Zhou, and S. Jiang, "Effect of thickness non-uniformity of large-area grating metal film on grating diffraction wavefront," *Optics & Laser Technology* **119**, 105675 (2019).
9. S. Zhang, X. Mi, Jirigalantu Qian Zhang, S. Feng, H. Yu, and X. Qi, "Groove shape characteristics of echelle gratings with high diffraction efficiency," *Opt. Commun.* **387**, 401–404 (2017).
10. D. Nevejans, E. Neefs, E. Van Ransbeeck, S. Berkenbosch, R. Clairquin, L. De Vos, W. Moelans, S. Glorieux, A. Baeke, O. Korabev, I. Vinogradov, Y. Kalinnikov, B. Bach, J.-P. Dubois, and E. Villard, "Compact high-resolution spaceborne echelle grating spectrometer with acousto-optical tunable filter based order sorting for the infrared domain from 2.2 to 4.3  $\mu\text{m}$ ," *Appl. Opt.* **45**(21), 5191–5206 (2006).
11. G. R. Harrison, "The Production of Diffraction Gratings I. Development of the Ruling Art," *J. Opt. Soc. Am.* **39**(6), 413–426 (1949).
12. W. R. Horsfield, "Ruling Engine with Hydraulic Drive," *Appl. Opt.* **4**(2), 189–193 (1965).
13. C. Mitchell, "Diffraction grating fabrication in Australia," *Spectrochimica Acta Part B: Atomic Spectroscopy* **54**(14), 2041–2049 (1999).
14. X. Mi, S. Zhang, X. Qi, H. Yu, H. Yu, Y. Lin, X. Yao, S. Jiang, and J. Zhou, "Effect of the changes in refractive index of air on grating diffraction wavefront, Optics Communications," *Opt. Commun.* **457**, 124716 (2020).
15. H. W. Babcock, "Control of a ruling engine by a modulated interferometer," *Appl. Opt.* **1**(4), 415–420 (1962).
16. G. R. Harrison, N. Sturgis, S. P. Davis, and Y. Yamada, "Interferometrically controlled ruling of ten-inch diffraction gratings," *J. Opt. Soc. Am.* **49**(3), 205–211 (1959).
17. G. R. Harrison and S. W. Thompson, "Large diffraction gratings ruled on a commercial measuring machine controlled interferometrically," *J. Opt. Soc. Am.* **60**(5), 591–595 (1970).
18. G. R. Harrison, S. W. Thompson, H. Kazukonis, and J. R. Connell, "750-mm ruling engine producing large gratings and echelles," *J. Opt. Soc. Am.* **62**(6), 751–756 (1972).
19. T. Kita and T. Harada, "Ruling engine using a piezoelectric device for large and high-groove density gratings," *Appl. Opt.* **31**(10), 1399–1406 (1992).
20. X. Mi, H. Yu, H. Yu, S. Zhang, X. Li, X. Yao, X. Qi, Bayinheshig, and Q. Wang, "Correcting groove error in gratings ruled on a 500-mm ruling engine using interferometric control," *Appl. Opt.* **56**(21), 5857–5864 (2017).
21. X. Mi, S. Zhang, X. Qi, H. Yu, H. Yu, and Y. Tang, "Ruling engine using adjustable diamond and interferometric control for high-quality gratings and large echelles," *Opt. Express* **27**(14), 19448–19462 (2019).
22. Z. Qu, "A fiber arrayed solar optical telescope," *Proceedings of the Conference Series of Astronomical Society of the Pacific* **437**, 423–431 (2011).
23. G. Dun and Z. Qu, "Design of the polarimeter for the fibre arrayed solar optical telescope," *Chinese Astronomy and Astrophysics* **53**(1), 342–352 (2012).
24. Z. Song and Z. Qu, "A Novel Scanning Method Applied to New-Style Solar Telescope Based on Autoguiding System," *Advances in Astronomy* **4575**, 679 (2018).